Elementary Implementation of VTK XML files
A FEMDEM Application

JOHN-PAUL LATHAM*†, ADO FARSI*†, and MICHAEL TRAPP*

A recent state-of the arts review by EU decision makers revealed that current building guidelines are not taking into account threats such as natural disasters and acts of terrorism, see [1]. Updating these guidelines requires accurate numerical models to quantify the resilience of building elements against explosive and projectile impact.

The Applied Modelling and Computation Group (AMCG) at Imperial College London has recently developed a novel coupled dynamic gas/solid FEMDEM code.

In this paper, this Y code is applied to simulate 2D projectile impact on laminated glass. Furthermore, a novel implementation is presented to prepare and write VTK output files. Before, obsolete external VTK libraries were required to visualise the code output.

The simulation results are not realistic, indicating errors in the preparation software or in the underlying code. The implementation of VTK files is successful and valid output files are produced. The files are visualisable using Paraview.

CCS Concepts: • **Applied computing** → *Engineering*.

*Imperial College London.
†Supervisor

Authors' address: John-Paul Latham, j.p.latham@imperial.ac.uk; Ado Farsi, ado.farsi@imperial.ac.uk; Michael Trapp, mt5918@ic.ac.uk.

Additional Key Words and Phrases: FEMDEM, VTK, Legacy, XML, base64, encoding

1 PHYSICS THEORY
1.1 Laminated Glass Model

Laminated glass is a sandwich structure of two brittle glass plies and an adhered polymer inter-layer (or inter-face) in between. The bonding between the glass and the inter-layer is without physical adhesive [2]. Secondary laminated glass consists of two such laminates, separated by a layer of air.

Advantageous properties of laminated glass include a relatively high penetration resistance [3], low weight [4] and the adherence of fractured glass fragments to the structure to reduce the risk of injuries[3, 5, 6, 7]. Breakage of the inner ply significantly reduces strength and facilitates a full collapse of the glass [6]. An optional back layer (usually poly-carbonate (PC) [8, 9]) improves structural stability and additional energy absorption [8, 10].

The prediction of crack initiation and propagation poses a significant challenge and requires ongoing research effort. Local stress intensification is caused by pre-existing micro-structural material flaws (inhomogeneities or discontinuities) such as micro-cracks and voids [11].

Many fracture models have been proposed. The Y code uses a local combined single and smeared crack model approach [12, 13], in which a single crack is replaced by a blunt crack band [14].
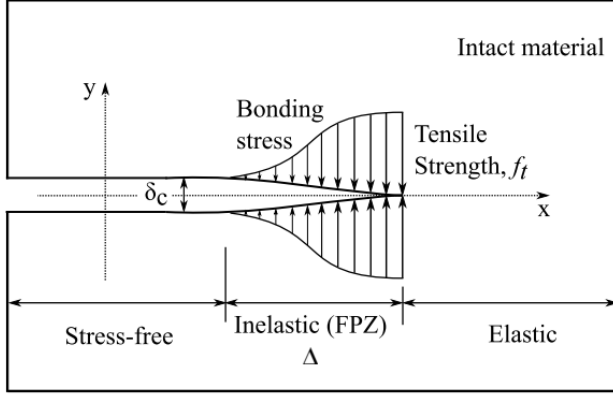

Fig. 1. Single Crack (Dugdale) Model. [15]

The single crack model in Fig. 1 assumes a crack tip located in a fracture process zone (FPZ). Plastic bonding stress $\sigma \leq f_t$ causes the crack tip to open up, up to a critical separation length $\delta = \delta_c$ [15].

To determine the bonding stress, the Y code adopts the `Mohr-Coulomb` constitutive model [13], described by

$$\tau = c + \sigma \tan\phi, \qquad (1)$$

with shear stress τ, normal stress σ, internal cohesion c and internal friction angle ϕ. The internal friction coefficient is given by

$$\eta = \tan\phi \qquad (2)$$

The stresses σ and τ correspond to normal and shear displacements δ_n and δ_s and tensile and shear strengths f_t and f_s. These material strengths are defined as the maximum strength in the stress-displacement diagram (Fig. 2), with maximum elastic displacement δ_p and critical displacement δ_s.
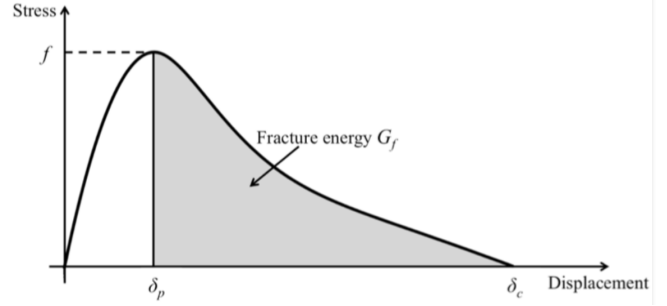

Fig. 2. Stress-displacement curve according to the single and smeared crack model. [13]

The fracturing in the strain-softening part is modelled using joint elements which are generated between two neighbouring shell elements. Cracks coincide with the element edges [15].

Further description is given for instance by Latham et al [13], Munjiza et al [14], Lei et al [16] and Chen and Chang [17].

1.2 Inter-layer Model

The task of the inter-layer is the absorption of impact energy and the maintenance of adhesion to the plies [4]. The inter-layer consists of one or more sheets. Common inter-layer materials include polymers such as polyvinyl butyral (PVB), thermoplastic polyurethane (TPU), and most recently `SentryGlas®Plus` (SGP) [18, 19].

Mechanical properties of the inter-layer are dependent on the fracture state of the laminated glass [20]. Prior to fracture, straining of the inter-layer is limited, permitting the application of linear visco-elastic laws. After the failure of the glass, the inter-layer is subject to large strains and linear visco-elasticity is no longer applicable. Instead, the inter-layer is modelled as a hyper-elastic material [21, 22]. Work done by stresses onto such materials only depends on the reference state X and the current state x, but not on the load path (Fig. 3). Deformation from X to x is described by a deformation gradient [23]

$$F = \frac{d\varphi}{dX} \qquad (3)$$

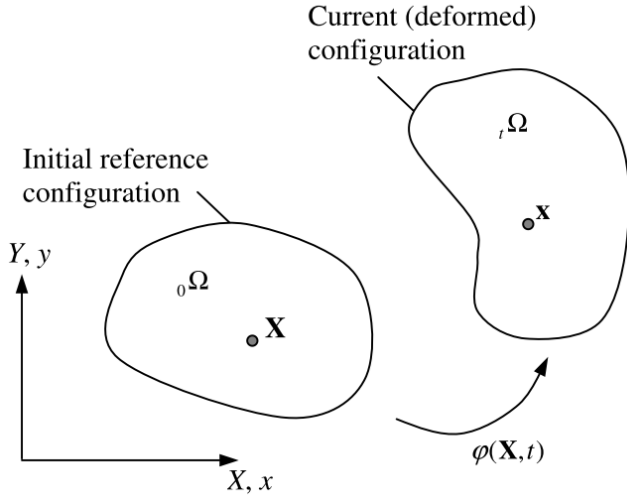with mapping function φ mapping from X to x.

Fig. 3. Deformation from reference to current state. [23]

Hyper-elastics are mathematically described by a characteristic strain energy density function W. One of the simplest hyper-elastic models is the Neo-Hookean model [21] whose characteristic function is given by

$$W = \frac{\mu_0}{2}(I_1 - 3) - \mu_0 \ln J + \frac{\lambda_0}{2}\ln^2 J, \qquad (4)$$

with Lamé constants λ_0 and μ_0 from the linearised theory, $J = |F|$ and first invariant $I_1 = C_{II}$ with right Cauchy stress tensor [21]

$$C_{ij} = F_{Ii}\, F_{Ij}. \qquad (5)$$

Upper case indices refer to the reference configuration, while lower case indices refer to the current configuration.

Another common, simple hyper-elastic model is the Mooney - Rivlin model [24, 25]. The characteristic strain energy function for the compressible 2-Parameter Mooney - Rivlin model [25] is given by

$$W_2 = C_{10}\left(\bar{I}_1 - 1\right) + C_{01}\left(\bar{I}_2 - 1\right) + \frac{1}{d}(J - 1), \quad (6)$$

where C_{10} and C_{01} are adjustable parameters, $d = 2\,/\,K$ with bulk modulus K and $\bar{I}_1 = J^{-\frac{1}{3}} I_1$ and $\bar{I}_2 = J^{-\frac{1}{3}} I_2$ are deviatoric invariants [24]. The second invariant is given by

$$I_2 = \frac{1}{2}\left(C_{JJ}^2 - C_{IK}C_{KI}\right). \qquad (7)$$

Other hyper-elastic models [24] include a more general polynomial model, Arruda-Boyce, Ogden and Yeoh. For the polynomial model, customized coefficients [2] already exist in the literature, specifically for laminated glass.

Modelling the occurence of fracture needs to be permitted for the inter-layer as well, as fracturing of the inter-layer is possible. This consideration necessitates the extension of the smeared single and combined fracture model to the inter-layer.

2   NUMERICAL MODELLING THEORY

2.1   FEMDEM Model

The combined finite-discrete element method, FEMDEM or FDEM[3, 12, 14, 17, 19, 26, 27, 28, 29, 30], contains discrete element that interact with neighbouring discrete elements. In addition, each discrete element is discretised into finite elements. Each finite element mesh captures the deformability of a discrete element.

Fracture and fragmentation is modelled as a transition from continua to discontinua. It is also in principle possible to imagine an inverse process of particles merging together.[14]

Based on the 3D FDEM code Y3D by Munjiza et al [12, 14, 26], Xiang et al [31] added many detailed improvements and features to the code. The new model, Solidity, is capable of creating realistic coupled multi-physics simulations. In contrast to

conventional models, Solidity is not reliant on element deformability restriction constraints (due to the locking problem) and uses simpler triangular, quadratic and tetrahedral elements [13].

2.2 Governing Equations

The governing equations for the finite element calculations in the FEMDEM method are the equations of motion. The equations are given by

$$M\ddot{x} + \mu\dot{x} + f_{int} = f_{ext} = f_l + f_b + f_c, \qquad (8)$$

with lumped nodal mass matrix M, nodal displacements x, viscosity μ, internal nodal forces f_{int} and external nodal forces f_{ext}. External forces contain consist of external loads f_l, bonding forces f_b and contact forces f_c. Internal forces f_{int} are generated by element deformation. FEMDEM systems solve these equations via explicit time integration using the forward Euler method [16].

2.3 Contact Detection

The combination of discrete and finite elements is established via an interaction algorithm [16]. This algorithm consists of contact detection [32] and contact interaction [28]. Contact detection is carried out using search algorithms.

The contact detection algorithm detects couples of discrete elements close to each other by eliminating couples of discrete elements that are too far from each other to be in contact. In other words, contact detection avoids processing contact interaction when there is no contact. This reduces CPU requirements and processing run time [14].

Contact interaction is only considered for discrete elements which are within a buffer size b of each other, given by

$$b = 0.1 \, \Delta_{min}, \qquad (9)$$

where Δ_{min} is the minimum edge[1].

---

[1]minimum element side length, minimum size

2.4 Contact Interaction

Penetration of a contractor[2] body into a target[3] body is implemented in the Y code by the `potential contact force method`, see Fig. 4 [14]. Assumption of a conservative force field enables a description of the contact forces using potentials,

$$f_c^{2D} = -f_t^{2D} = \oint_{\Gamma_{\beta t \cap \beta c}} n_\Gamma \, (\varphi_c - \varphi_t) \, d\Gamma, \qquad (10)$$

$$f_c^{3D} = -f_t^{3D} = \int_{S_{\beta t \cap \beta c}} n_S \, (\varphi_c - \varphi_t) \, dS, \qquad (11)$$

with force potentials φ and outward unit normal n to the penetration boundary Γ or surface area S.
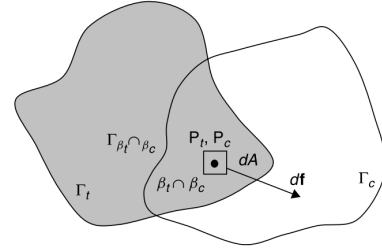
Fig. 4. Infinitesimal overlap of contractor and target body. [14]

The penetration distance d for each case is given by [14]

$$d = \frac{\sigma \, h}{p}, \qquad (12)$$

with applied pressure σ, element height h and penalty factor p.

The penalty factor p is given by

$$p = \alpha \, E, \qquad (13)$$

with Young's Modulus E and a constant α (in this paper: $\alpha = 10$) to regulate penetration.

---

[2]index c

[3]index t

Contact damping (Rayleigh damping, viscous damping) due to plastic deformation, breakage of surface asperities, etc. is given by [14]

$$\sigma_C = 4\,\xi\,\frac{\sqrt{p/\rho}}{h}\dot{d}, \qquad (14)$$

with damping ratio $0 \le \xi^4 \le 1$ and finite element density ρ.

The mass damping coefficient is given by

$$\zeta = \sqrt{E\,\rho} \qquad (15)$$

3 NUMERICAL MODEL APPROACH
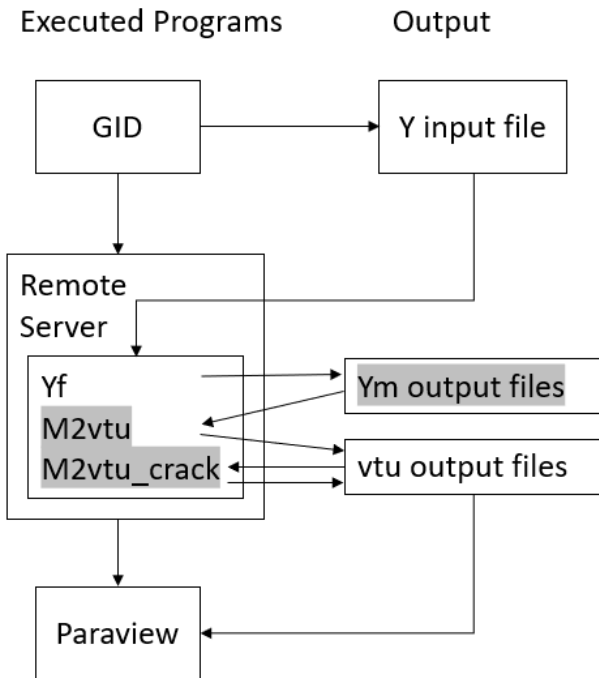
3.1 Workflow

Fig. 5. Workflow of generating a simulation

The workflow is illustrated in Fig. 5. The grey shaded items are removed using this paper such that the Yf code now generates the VTK output

---

[4] describes energy dissipation

files directly. The workflow was tested on Ubuntu 18.04.2 LTS subsystem for windows 10.

A 2D input Y file is generated on Windows 10 using the open source pre-processor CAD software GID [33]. It is possible to instead import the geometry from other CAD software, such as AutoCAD.

The input file is compiled using three binary files Yf, m2vtk and m2vtk_crack, which constitute the Y2D code. The program may be obtained from the AMCG at Imperial College London. Code execution requires obsolete VTK 5.8 libraries and the obsolete operating system Ubuntu 14.4. Tests were conducted on two remote servers, the high performance computing (HPC) system at Imperial College and a private remote university server.

The code outputs .vtu files which compose a time series simulation. The output is visualised using the open source software Paraview.

3.2 Geometry Setup

The input file contains the model including the geometry, constraints, materials, as well as the simulation parameters. The majority of modelling parameters are adduced from the literature. A list of material parameters is given in appendix table 1. A list of input file simulation parameters is provided in appendix Table 2. Auxiliary parameters are provided in Table 3.

Fig. 6. 2D geometry of the laminated glass structure and projectile [17]

Fig. 6 illustrates the 2D geometric setup. The figure shows the initial state of the spherical projectile (yellow) immediately before impact on the laminated glass (impactor glass plies in red, inner glass ply in blue, inter-layer in green). The glass is fixed via a support system (brown). The support structure is not modelled for now and is replaced

with no-velocity boundary conditions acting on the sides of the glass plies.

In real-world applications, the dimensions of the inter-layer are smaller compared to the glass plies. Therefore, a translational degree of freedom in the y-direction exists for the inter-layer. This effect will also need to be considered in this paper.

Critical flaws, which cause complete structural failure, are usually found on the cut and machined glass edges [34]. Based on this consideration, the boundary structure layout requires special care. A project task remains to determine a realistic boundary structure to be applied.

Modifications to this preliminary geometric setup will include changes to the shape of the projectile, as well as changes to the thickness of the layers. A potential consideration is to model the projectile as firearm ammunition instead of a circle (or sphere). A symmetry boundary condition may be applicable and only half of the laminate may need to be modeled.

The dimensions of the glass plate is set to 2000 mm× 2000 mm in order to avoid anisotropic effects. The thickness of the glass plies is set to 2 mm and 0.76 mm for the inter-layer. For now, a PVB material is chosen for the inter-layer.

The preliminary mesh for all bodies consists of triangular elements. For the 3D model, tetrahedral elements [17] are to be considered. The preliminary element size is 1 mm. Necessary modifications include reducing the number of elements for the projectile, as it is not of interest for the analysis and increasing the element size for far-field mesh elements for the plies and inter-layer. Potentially, differently shaped elements are more optimal for the results. The glass and inter-layers need to consist of several element layers to enable a more precise analysis.

3.3 Material Parameters

Table 1 lists the material parameters for glass, PVB, steel and rock. The literature provides values for most of the quantities, although they are extremely diverse in some cases. The values used in this paper are marked bold. The elastic and contact penalties are evaluated using Eq. 13.

3.4 Problem Parameters

The radius of the steel sphere (or circle) is set to 2.5 mm. The critical time step [42][9] is set accordingly to

$$\Delta t_{\mathrm{crit}} = \sqrt{\frac{V_{\mathrm{e}}{}^{10} \, \rho^{11}}{p}} = \sqrt{\frac{0.000413 \cdot 7.8 \cdot 10^3}{4 \cdot 10^{11}}} \, \mathrm{s} \,. \tag{16}$$

The acceptable time step Δt is given by

$$\Delta t = \lfloor \Delta t_{\mathrm{crit}} \rfloor = 3\mathrm{e} - 6\,\mathrm{s}\,, \tag{17}$$

, where $\lfloor \, \rfloor$ denotes the floor operator. To simulate real time $t = 10\,\mathrm{s}$, the maximum number of time steps required [42][9] is given by

$$n_{\mathrm{t}} = \frac{t}{\Delta t} = \frac{10\,\mathrm{s}}{3\,\mathrm{e} - 6\,\mathrm{s}} = 1\mathrm{e}6 \,. \tag{18}$$

3.5 Verification

Meeting specified accuracy standards [1] requires verification of the numerical model by use of data from numerical experiments. Physical experiments involving the breakage of glass by projectiles or shock blasts require special safety arrangements. Air blast impact experiments are being conducted

---

[5]for reference

[6]Rayleigh damping, viscous damping

[7]not relevant for glass, PVB and steel

[8]at laboratory conditions

[9] for inquiries concerning this reference please contact the AMCG at Imperial College London

[10]volume (in m^3) of the smallest finite element, without units

[11]density (in kg/m^3) of the material of the smallest finite element, without units

Table 1. List of Y2 input material parameter values.

Property	Glass	PVB	Steel Projectile	Rock[5]
Density ρ $\left[\text{kg/m}^3\right]$	2500 [17, 24, 30, 35, 36]	870 [30] **1100** [17, 35, 36] 1105e3 [17]	7800 [17]	2700
Young's Modulus E [Pa]	**7e10** [17, 35, 36] 7.409e10 [30] 7.41e10 [17] 7.5e10 [24]	**1e8** [17] 2.2e2 [36] 5e10 [30]	2e11 [17]	3e10
Poisson's Ratio ν	0.2 [17, 30] 0.21 [24] 0.3 [17] 0.22 [35] **0.23** [36] 0.25 [17]	0.42 [17] 0.45 [24] 0.48 [30] 0.49 [32] **0.495** [36]	0.29 [17]	0.205
Mass damping coefficient μ^6 (see Eq. 15)	0	0	0	0
Elastic penalty term (see Eq. 13)	7e11	1e9	2.0e12	3.0e11
Contact penalty (see Eq. 13)	7e11	1e9	2.0e12	3.0e11
Mode I energy rate G_I $\left[\text{J/m}^2\right]$	**10** [35] 3.9 [17] 4.0 [17]	2.8e3 [37] **20** [17]	1.9e5 [38]	20.0
Mode II energy rate G_II $\left[\text{J/m}^2\right]$	50 [35]	2.8e3	1.9e5	100.0
Mode III energy rate G_III $\left[\text{J/m}^2\right]$	50 [35]	2.8e3	1.9e5	100.0
Tensile Strength σ [Pa]	6e7 [32] 3e7 [17] **3.46e7** [17]	**2e7** [39] 1.862e7 [17]	1e7 [4]	4e6
Shear Strength τ [Pa]	17.9 [17]	17.9 [17]		
Internal friction coefficient η (Eq. 2)	0.1 [32]	0.7 [20]	0.15 [40]	0.6
Internal cohesion c [Pa] (Eq. 1)	7e10	2.2e2	2e11	8e6
Pore fluid pressure[7] [Pa]	0	0	0	0
Joint friction coefficient[7]	0.6	0.6	0.6	0.6
Joint roughness coefficient JRC_0 [7, 8]	15	15	15	15
Joint compressive strength JCS_0 [7, 8] [MPa]	120	120	120	120
Joint sample size [m][7]	0.2	0.2	0.2	0.2
Interface friction	0.1 [32]	0.62 [41]	0.44 [41]	0.6
2D Problems	plane strain			

Table 2. List of Y2D input simulation parameter values.

Parameter	Value
Maximum number of timesteps n_t (Eq. 18)	2e6
Current number of timesteps	0
Restart file saving frequency	1e2
Gravity in X Direction (m/s2)	0
Gravity in Y Direction (m/s2)	0
Gravity in Z Direction (m/s2)	−9.8
Timestep (s) (Eq. 17)	1e − 6
Output frequency	2e3
Current number of iterations	0
Gravity setting stage (s)	0
Load ramping stage (s)	0
Maximum dimension (m)	10
Maximum force (N)	1e6
Maximum velocity (m/s)	100
Maximum stress (Pa)	1e8
Maximum displacement (m)	0.1
Minimum joint aperture (m)	1e − 7
Maximum contacting couples	1e7
Buffer Size b for NBS (m) (Eq. 9)	7.60e − 5
Accuracy (bit)	32
Joint friction model	Coulomb
Initial aperture correlation	roughness

Table 3. List of auxiliary parameter values (to calculate simulation parameter values).

Parameter	Value
Total minimum element volume V_e (m^3)	1.00e − 07
Total minimum edge Δ_{min} (m)	4.13e − 04
Total real simulation time t (s)	10
Critical time step glass (s) (Eq. 16)	2e6
Critical time step steel (s) (Eq. 16)	2e6
Critical time step PVB (s) (Eq. 16)	2e6
Overall Mesh size (m)	2.5e − 4
Mesh size projectile (m)	2.5e − 4
Mesh size plies (m)	2.5e − 4
Mesh size inter-layer (m)	2.5e − 4

such as bird impact [44] causes the projectile to undergo extensive deformation.

Relevant parameters of the impact projectile include the normal velocity [4, 45, 46, 47], the mass [46, 47], the angle [45, 46, 47], the shape [47] and the size [4]. Relevant parameters for the outer glass ply include its dimensions [19], its mass, the support conditions [19] and the make-up [19]. For the inter-layer, the material [9, 18, 19], thickness [7, 19, 46] and temperature [18, 48] are relevant.

Low velocity ($\approx 20\,\text{m/s}$) hard impact experiments include the use of projectiles in form of road construction chippings [45], ballistics [9], drop-down weights [19, 32, 49], aluminum projectiles [49] and steel balls [6, 19, 50]. High velocity (around $180\,\text{m/s}$) soft impact experiments include the use of silicon rubber projectiles [44] and gas guns [18].

Wang et al [19] found that the panel size had an inferior effect on the breakage resistance [19]. Similarly, Monteleone et al [9] found that only a local area of the ply around the impact absorbed the impact energy for high velocities.

Karunarathna [46] found that impact velocity and plate thickness contributed significantly towards the impact resistance, compared to impact mass

outdoors by service company Jabisupra [43] in cooperation with Imperial College London. The company is active in the field of envelope security and specialises in protecting infrastructure from certain threats. The data from Jabisupra is not expected to yet be ready and applicable for this project. Many other researchers have already conducted impact experiments in the past and a majority of the findings from these experiments are likely to be applicable to verify the model for this project.

Dynamic impact on laminated glass comprises hard and soft body impact [44]. Hard body impact such as ballistic impact [8] causes minimal deformation to the projectile, while soft body impact

and inter-layer thickness. Wang et al [19] found an increased inter-layer thickness to have a negative effect on energy absorption. Liu et al [51] established that the inter-layer thickness did not contribute towards energy absorption. Behr and Kremer [50] found an increased inter-layer thickness to better protect the inner ply. Kim et al [52] numerically optimised the PVB inter-layer constitution to prevent all damage to the inner glass ply.

Liu et al [51] numerically investigated the optimisability of the inter-layer in terms of energy absorption by simulating the impact of a human head. Zhang et al [48] investigated the influence of temperature on the inter-layer and found that a hybrid TPU/SGP/TPU inter-layer performed best over the entire range of tested temperatures.

4   COMPUTER SCIENCE APPROACH

The following definitions are adopted from the code:

```
1  #define FLT   float
2  #define INS   int
3  #define DBL   double
4  #define INT   long
5  #define UCHR  unsigned char
6  #define CHR   char
7  #define UINT  unsigned int
8  #define ULON  unsigned long
```

Listing 1 Data type definitions

4.1   VTK format

The Visualisation Toolkit VTK [53] is an extremely popular open source software for graphic visualisation of scientific data. VTK APIs are available in many different programming languages and facilitate the generation of VTK files. Until now, the Y code used the VTK API for programming language c to generate output files.

The required VTK version 5.8 library dependencies revealed themselves to be outdated and unobtainable. This limited the applicability of the entire

Y code to operating systems which support this obsolete version. Specifically, all attempts by the author to obtain such a version for testing were not successful. Rewriting the code using a newer VTK version (i.e. a newer VTK API) would only temporarily solve this problem.

To diversify application to a wider range of operating systems, it was deemed necessary to hard code the output without using VTK libaries. Aside from the partly ill-documented offical website [53], one of the only few reliable resources available is the Earth Models website by Bunge [54]. In what follows, the aim is to provide the reader with a more detailed and more in-depth description of the VTK format.

4.2   VTK legacy file format

The VTK legacy file format is sufficiently documented (see [53] for official documentation) and relatively easy to implement. On the downside, it only supports a minimal amount of features and is relatively inflexible. List. 1 in section 5 shows an example VTK legacy output file.

The header defines VTK version, file name, data encoding (ascii or binary) and dataset type [12] [53].

The data is divided into sections including points, cells, cell types. The section header contains the keyword along with the total amount of entities of the section. The data is written continuously using spaces as separators. [53]

Every section has additional unique formatting rules. The points sections requires an additional data type identifier (here: float) to correctly identify the coordinates data. [53]

---

[12]here: unstructured grid

The data in the cells section lists the node numbers of each element, appended to a number identifying the total amount of nodes of the element. [53]

The cell type section identifies the geometric shape of each element, given by an index. Each index is written on a separate line. [53]

4.3 VTK XML file format

Compared to legacy files, XML files are much more difficult to implement. An example is given in List. 2 in section 5.

The file is structured using nested keyword headers which are enclosed in angle brackets ("<" and ">"), according to XML language. Text indentation is not required but enhances readability.

Keyword headers are opened using <keyword> and closed using </keyword>. Keywords which do not contain any sub-keyword headers are opened and closed in one line using <keyword\>. Keyword headers usually contain additional mandatory and optional keywords in the format of option="value" [53].

The file header specifies versions, VTK file type and byte_order [13] [53]. Big endian byte order was not tested, as such operating systems were not available for testing.

Depending on the specified VTKFile type, a unique set of sub-keyword headers is used. For the Unstructured_Grid VTK file type chosen here, the file content is structured using <Piece>. Within this header, it is required to specify the number of points and cells (elements) using NumberOfPoints and NumberOfCells ↪ [53].

<Piece> contains definition of <Points> and <Cells ↪ >, among other optional keyword sub-headers. <Points> expects exactly one <DataArray> containing the nodal coordinates. <Cells> expects one < ↪ DataArray> each for the cell connectivity (node configuration of each cell), the cell offsets (offsets in the cell connectivity list), as well as the cell type (cell shape index, see [53]) [54].

The data, listed after <DataArray> includes type (data type), Name, NumberOfComponents, format, RangeMin ↪ and RangeMax.

RangeMin and RangeMax indicate the minimal and maximal values of the data and are optional[14]. Simple array search functions were implemented in order to find the individual values.

Name specifies a unique name, enclosed by "", for the data set. The data array contained in <Points> requires no name. The data arrays enclosed by < ↪ Cells> require fixed names Name="connectivity", Name="offsets" and Name="types" [53].

format specifies the encoding of the data.

In the case format="ascii", the data is provided in decimal form, delimited by spaces, similar to section 4.2 [54]. Specifying an inappropriate data type for this format will not leave the data completely unusable, although induced type casting may yield unexpected results. The dependence on spaces as delimiters is highly impractical when transferring files between different operating systems and applications.

A more robust option is given by format="binary ↪ ". Characters such as "<" (binary encoding of 0b00111100=d060) may potentially appear in binary encoded data. As these characters compose XML keyword headers, binary encoding is not realizable [54]. Thus, the data is encoded to base 64 (b64) (see 4.4).

---

[13]endianess, here: little endian

[14]confirmed by tests

For b64 encoding, a data header needs to be prepended to the data. The data header is always of type `int32` (data size: 4 bytes) and specifies the data size, i.e. the amount of binary bytes of subsequent data. The data size is not to be confused with the length of the printed b64 encoded data string in the output file, which is insignificant for now. The data size rather refers to the size of the binary data array in `bytes`, stored as specified by the datatype in the header. Specifying a data `type` of a different `byte` size for this format produces errors and renders the data useless.

As an example, consider a `float32` array which contains 100 data values. The corresponding header is given by:

$$h = 100 \, \frac{32 \, \text{bits}}{8 \, \text{bits/byte}} = 400 \, \text{bytes} \qquad (19)$$

The header then needs to be encoded to b64, separately from the data. The encoded header string is immediately followed by the encoded data string, without any delimiters. Considering the fact that the data header type is fixed, the b64 encoded data header string length is always the same. Thus, no additional offset is necessary to specify the positional onset of the data after the data header [54].

Instead of supplying the data inline, it is possible to append data once, to an `<AppendedData>` section at the end of the file. This is achieved by specifying option `format="appended"` for each data array keyword header and providing an `offset` each time.

In doing so, the entire data is provided in a single long b64 encoded string, appended to an underscore "_". Like in the inline format, each encoded data string must be prepended by a b64 encoded header, which specifies the size of the following unencoded data section in bytes. The headers and the data sections are encoded separately each, without any delimiters between headers and data sections.

The offset value provided in each `<DataArray>` specifies the amount of bytes of unencoded data after the underscore to the beginning of the corresponding header. The method of evaluation of header offsets is illustrated in Tab. 4.

In Tab. 4, the header offset of the first header is always 0. As the unencoded header is always an `int32` of size 4 bytes, the first data offset is 4. For a data array with 1926 values and data type size 8 bytes (e.g. `float64`), the data size in `bytes` amounts to $1926 \cdot 8 \, \text{bytes} = 15408 \text{bytes}$. The number of values is comprised by the number of components and the number of points, i.e. $3 \cdot 642 = 1926$. The next header offset is evaluated by adding the data size to the data offset, i.e. $4 + 15408 = 15412$. The remaining offset values are evaluated accordingly.

4.4 Base 64 encoding

The output data consists of one- and two-dimensional **int** and **float** arrays containing nodal properties, elemental properties and flags. The computer stores the data in binary form, according to byte order (endianess) of the operating system at hand.

float numbers are usually stored in IEEE-754 format [55]. As the numbers are stored internally, the exact manner of storage is theoretically not significant as long as the position (the significance) of the bits in binary-stored **float** is not being violated.

As the base64 encoding function takes in a contiguous `CHR*` array, the data needs to be segmented into bytes. For the `INS` data header, this simply involves conversion from a 4-byte `int32` to 4 `CHR` bytes. The segmentation process for arrays is illustrated in Fig. 7. The array is segmented into single bytes, rearranged in groups of 3 bytes and again rearranged in groups of 6 bits. The 6-bit groups are encoded to characters and compose the encoded string.

As an example, the implementation approach is discussed by use of the 2-dimensional contact force

Table 4. Breakdown of offset values for an example output file with 642 points and 1280 cells. The desired (header) offsets are given in column 2.

Name	header offset	data offset	data size	data type size	values	components	points/cells
Points	0	4	15408	8	1926	3	642
Connectivity	15412	15416	15360	4	3840	3	1280
Offsets	30776	30780	5120	4	1280	1	1280
Types	35900	35904	1280	1	1280	1	1280
Points s	37184	37188	5136	8	642	1	642
Points v	42324	42328	15408	8	1926	3	642
Points n	57736	57740	15408	8	1926	3	642
Density	73148	73152	5136	8	642	1	642

array. A complete implementation can be found in file `Yod.c`. In a first step, 2-dimensional arrays are reduced to contiguous one-dimensional arrays (List. 2).

```
1  DBL *cf; //contact force
2  INS i, j, k;
3  INS header;
4  header = sizeof(DBL) * ydn->nnopo * ydn->
       ↪ nnodim;
5  cf = malloc(header);
6  k = 0;
7  for (i = 0; i != ydn->nnopo; i++){
8    for (j = 0; j != ydn->nnodim; j++){
9      cf[k] = ydn->d2nfcon[j][i];
10     k++;}
11   cf[k] = ydn->d2nfcon[j][i];
12   k++;}
```

Listing 2 Converting 2-dimensional array to 1-dimensional array

In List. 2, ydn->nnopo denotes, in the class "**Y** **d**atabase of **n**odes", the current **n**umber of **nodal po**ints. ydn ↪ ->nnodim denotes the current **n**umber of **no**dal **dim**ensions (2) and ydn->d2nfcon denotes the **d**ouble **2**-dimensional **n**odal **f**orce of **con**tact.

As a result, the data is now stored in a contiguous one-dimensional array of `float64` and now needs to be segmented into bytes.

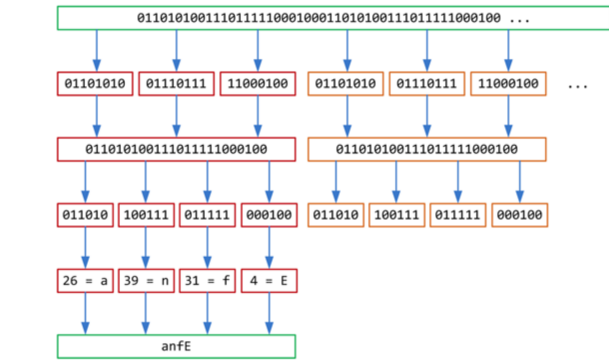A first possible strategy is to apply simple data type casting, see List. 3.

Fig. 7. Subsequent conversion of binary data to bytes, bit sextets, and encoded characters [56].

```
1  FLT floats[4] = {1, 2, 3, 4}
2  //actual array is of variable size;
3  CHR *bytes = (CHR *) floats;
```

Listing 3 Segmentation approach via type casting with pointers

The `CHR* bytes` array could then be passed on to the encoding function. Test showed that this strategy seems to only work if the array to type cast does not contain any data before type casting. Thus, this approach is not appropriate here.

A second possible strategy is to declare a **union**, see List. 4.

```
1  union INTToCHR {
2    INS i;
```

```
3    CHR *c[sizeof(INS)];};
```

Listing 4 Segmentation approach via a union

Here, both `i` and `c` refer to the same location in memory. This approach potentially works for a single **float**. As the `CHR*` arrays would need to be concatenated dynamically, this approach is (according to the author's opinion) not appropriate either. Test which were carried out using this strategy showed inconsistent outputs, indicating that the prompted data may not be contiguously stored.

A third strategy for dividing the data arrays into bytes uses a combination of `malloc` and `memcpy`, see List. 5.

```
1    CHR *bytes;
2    bytes = malloc(header);
3    memcpy(&bytes[0], cf, header);
```

Listing 5 Segmentation approach via memcpy

Testing confirmed that this method is successful. The `byte` array now contains the floats in contiguous order in binary form, stored as bytes.

The prepared data is passed to the base 64 encoding function `b64enc` in file `Yod.c`. The function takes some `CHR*` array `src` of length `len` as input, encodes it byte for byte and outputs character for character into the VTK output file `fout`.

The core of the algorithm (List. 6) was adopted from Malinen [57].

```
1    while (end - in > 2){
2      putc(enc[in[0] >> 2], fout);
3      putc(enc[((in[0] & 0x03) << 4) } (in[1] >>
          ↪    4)], fout);
4      putc(enc[((in[1] & 0x0f) << 2) } (in[2] >>
          ↪    6)], fout);
5      putc(enc[in[2] & 0x3f], fout);
6      in += 3;}
7
8    if (end - in){
9      putc(enc[in[0] >> 2], fout);
10     if (end - in == 1){
11       putc(enc[(in[0] & 0x03) << 4], fout);
12       putc('=', fout);}
13     else{
14       putc(enc[((in[0] & 0x03) << 4) } (in[1]
          ↪    >> 4)], fout);
15       putc(enc[(in[1] & 0x0f) << 2], fout);}
16     putc('=', fout);}
17   return;}
```

Listing 6 b64 algorithm

In List. 6, `in` and `end` are `CHR*` pointers which point to the beginning and end of the input array. Converting to base 64 requires rearranging the input in chunks of 6 bits. Each of these 6-bit chunks produces a value $v < 64 = 0b1000000$ and is able to be converted to one of 64 unique characters from the encoding array

```
CHR* enc = "ABCDEFGHIJKLMNOPQRSTUVWXYZ"
"abcdefghijklmnopqrstuvwxyz0123456789+/" .
```

For every 3 bytes (or 24 bits), the algorithm produces 4 groups of 6 bits, i.e. 4 characters. The bits are extracted continuously via bit shifting. As mentioned before, the position or significance of the bits in the byte must not be violated. In other words, the value of the bit must not get lost through bit shifting. The algorithm is now explained in detail:

In line 2, the first 6 bits of the current character `in[0]` are extracted by bit shifting to produce the first 6-bit chunk. The value of this chunk is used to produce the index of the corresponding character in the encoding array `enc`.

The last two remaining bits of the current input character `in[0]` are evaluated and bit shifted in line 3 to account for the first 2 significant bits of the next 6-bit chunk. The 4 missing bits to complete the 6 bits are extracted from the first 4 bits of the second character `in[1]`, again by bit shifting.

In line 4, the 4 remaining bits from the second input character `in[1]` make up the first four bits of the next 6-bit chunk. The missing 2 bits of the 6-bit chunk are extracted from the third input character

`in[2]`. This leaves 6 bits of the third input character remaining, making up another 6-bit chunk, as implemented in line 5.

If the input array length `len = end - in` is not divisible by 3, padding characters are required. The amount of padding padding depends on the amount of remaining input byes to complete a group of three input bytes. If len % 3 == 1, two padding characters '==' are appended to the encoded string. If len % 3 == 2, one padding character '=' is required. The algorithm is given in List. 6, lines 8-17.

Writing the output characters to a buffer instead of using `putc` reduces the amount of times of invoking the I/O buffer and may save computational time. This alternative was discarded as it did not provide any significant advantage in terms of computational costs in this minimal example.

5 RESULTS

5.1 Simulation

Fig. 8 shows snapshots of the simulation of an initial test geometry at initial and final time steps.
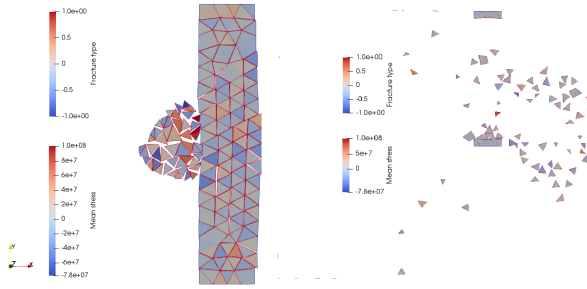

Fig. 8. Snapshots of simulation setup of a test geometry, at initial and final time steps.

Fig. 9 shows a snapshot of the simulation of the final geometry at the final time step.

5.2 VTK implementation

```
1   # vtk DataFile Version 5.8
2   CODED
3   ASCII
4   DATASET UNSTRUCTURED_GRID
5   POINTS 20 float
6   -1.000000 1.000000  0.000000 1.000000  0.000000
    ↪   1.000000  -1.000000 0.000000  0.000000
    ↪   0.000000  0.000000 0.000000
7   1.000000 1.000000  1.000000 0.000000  0.000000
    ↪   -0.000000  0.000000 1.000000  -1.000001
    ↪   0.000000  0.000000 1.000000
8   -1.000001 1.000000  -1.000001 0.000000  1.000001
    ↪   1.000000  0.000000 1.000000  1.000001
    ↪   0.000000  0.000000 -0.000000
9   1.000001 0.000000  0.000000 1.000000
10  CELLS 56
11  3 14 15 16
12  3 17 18 19
13  3 8 9 10
14  3 11 12 13
15  3 8 9 9
16  3 9 10 13
17  3 10 8 8
18  3 11 12 12
19  3 12 13 13
20  3 14 15 15
21  3 15 16 18
22  3 16 14 14
23  3 17 18 18
24  3 19 17 17
25  CELLTYPE 14
26  8
27  8
28  8
29  8
30  8
31  8
32  8
33  8
34  8
35  8
36  8
37  8
38  8
39  8
```

Listing 1. Example VTK legacy ascii encoded file

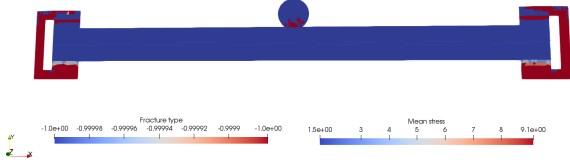Fig. 9. Snapshot of simulation setup as described in section 3 at final time step

```
1  <?xml version="1.0"?>
2  <VTKFile type="UnstructuredGrid" version="0.1"
   ↪   byte_order = "LittleEndian">
3    <UnstructuredGrid>
4      <Piece NumberOfPoints="20"
       ↪   NumberOfCells="14">
5        <Points>
6          <DataArray type="Float32"
           ↪   NumberOfComponents="3"
           ↪   format="binary"
           ↪   RangeMin="-1.000001"
           ↪   RangeMax="1.000001">
7            8AAAAA==AACAvwAAgD8AAAAAAAAAAAAgD8AAAA⌋
             ↪   AAAAAAAAAAgD8AAAAAAACAvwAAAAAAAAA⌋
             ↪   AAAAAAAAAAAAAAAAAAAAAAAAAAAAAAAAA⌋
             ↪   AAACAPwAAgD8AAAAAACAPwAAAAAAAAA⌋
             ↪   AAAAAAEdnLK0AAAAAAAAAAAAAAgD8AAAA⌋
             ↪   ACACAvwAAAAAAAAAAAAAAAAAAgD8AAAA⌋
             ↪   ACACAvwAAgD8AAAAACACAvwAAAAAAAAA⌋
             ↪   ACACAPwAAgD8AAAAAAAAAAAAAgD8AAAA⌋
             ↪   ACACAPwAAAAAAAAAAAAAAAAEdnLK0AAAA⌋
             ↪   ACACAPwAAAAAAAAAAAAAAAAAAgD8AAAAA
8          </DataArray>
9        </Points>
10       <Cells>
11         <DataArray type="Int64"
           ↪   Name="connectivity"
           ↪   NumberOfComponents="1" RangeMin=""
           ↪   RangeMax="" format="binary">
```

```
12           UAEAAA==DgAAAAAAAAPAAAAAAAAABAAAAAAAAA⌋
             ↪   AEQAAAAAAAASAAAAAAAAABMAAAAAAAA⌋
             ↪   ACAAAAAAAAAAJAAAAAAAAAAoAAAAAAAA⌋
             ↪   ACwAAAAAAAAAMAAAAAAAAAA0AAAAAAAA⌋
             ↪   ACAAAAAAAAAAJAAAAAAAAAAkAAAAAAAA⌋
             ↪   ACQAAAAAAAAAKAAAAAAAAAA0AAAAAAAA⌋
             ↪   ACgAAAAAAAAAIAAAAAAAAAAgAAAAAAAA⌋
             ↪   ACwAAAAAAAAAMAAAAAAAAAAwAAAAAAAA⌋
             ↪   ADAAAAAAAAAANAAAAAAAAAA0AAAAAAAA⌋
             ↪   ADgAAAAAAAAAPAAAAAAAAAA8AAAAAAAA⌋
             ↪   ADwAAAAAAAAAQAAAAAAAAABIAAAAAAAA⌋
             ↪   AEAAAAAAAAAAOAAAAAAAAAA4AAAAAAAA⌋
             ↪   AEQAAAAAAAASAAAAAAAAABIAAAAAAAA⌋
             ↪   AEwAAAAAAAAARAAAAAAAAABEAAAAAAAA
13         </DataArray>
14         <DataArray type="UInt32" Name="offsets"
           ↪   NumberOfComponents="1" RangeMin=""
           ↪   RangeMax="" format="binary">
15           OAAAAA==AwAAAAYAAAAJAAAADAAAAA8AAAASAA⌋
             ↪   AAFQAAABgAAAAbAAAAHgAAACEAAAAkAA⌋
             ↪   AAJwAAACoAAAA=
16         </DataArray>
17         <DataArray type="UInt32" Name="types"
           ↪   NumberOfComponents="1" RangeMin=""
           ↪   RangeMax="" format="binary">
18           OAAAAA==BQAAAAUAAAAFAAAABQAAAAUAAAAFAA⌋
             ↪   AABQAAAAUAAAAFAAAABQAAAAUAAAAFAA⌋
             ↪   AABQAAAAUAAAA=
```

```
19         </DataArray>
20       </Cells>
21     </Piece>
22   </UnstructuredGrid>
23 </VTKFile>
```

Listing 2. Example VTK XML file with b64 inline encoding

An example VTK legacy output file is given by List. 1. An example VTK XML b64 inline encoded output file is given by List. 2.

6 DISCUSSION

6.1 Simulation

The simulation clearly only produces realistic results for simple geometry setups.

Simulation results for more complex geometries are not realistic. Here, the projectile of prescribed

material steel locally deforms on impact on the glass, while the glass ply does not show any reaction to the impact.

A likely cause might be implementation issues in the pre-processing softwares. The pre-processors GID and AutoCAD proved to be extremely unreliable.

The input file prepared using GID presumably contained contradictory definitions compared to the code. For example, the nodes which make up each element seemed to be defined in oppose rotational direction GID. It may be possible that importing geometries from AutoCAD produced this error. Another possibility may be that the preprocessor may produce different outputs on different operating systems. As code for these programs is not publicly available, further investigation is difficult or imossible.

As the pre-processor GID proved to be unpredictable on different operating systems and code is not available, it is of significant importance to replace this software with more reliable alternatives such as Gmesh [58].

Another plausible cause might be errors in the original code, made by previous programmers. The code can clearly not be executed in a clean environment, such as the Travis environment in a Github repository.

```
1  JCS0=d1pjcs[propID];
```

Listing 7 Memory allocation error for variable JCS0 in file Yrd.c

One such error occurs in line 676 in file Yad.c, see List. 7. There seems to be a memory allocation error, although the circumstances are not quite clear to the author.

Another error occurs at the beginning of the program in line 733 in file Yrd.c, see List. 8.

```
1  #define SETLINEBUF(fcheck) setvbuf((fcheck),
   ↪   NULL, _IONBF, 0); //definition
2  SETLINEBUF(ydc->fcheck); //line 733
```

Listing 8 SETLINEBUF Error in file Yrd.c

The command setvbuf((fcheck), NULL, _IONBF, ↪ 0) presumably assigns an empty buffer NULL to some file ydc->fcheck. However, the specifics and the purpose are again unclear to the author.

6.2   VTK Implementation

It is extremely inconvenient and inefficient to debug the code using the HPC system by evaluating the error files of submitted jobs. The only sensible solution was to remove the dependencies such that the code is able to be run locally.

The elementary implementation to generate valid VTK output files is successful. Both types of VTK output files are able to generated and simulated.

The results have wide-ranging effects for further research.

The results can be applied to the Y3D code to also simulate three-dimensional output. The algorithm for the Y3D code is estimated to be of similar nature as for the Y2D code. It is expected that only minor adjustments to the output data are necessary.

The output algorithm may be further improved by the implementation of a compression algorithm to compress to the VTK XML files. This is indicated in the file by adding the option

```
compressor="vtkZibDataCompressor"
```

to the header [53]. Bunge [54] provides a promising algorithm, but it remains to be revised, adjusted and implemented.

Most significantly, the modified code removes the obsolete VTK dependency, which until now prevented the Y2D program from being run locally.

This paves the way for program debugging and testing. With the results from this paper, the program can be debugged without first being transferred to remote systems such as the HPC system.

The next step should be to pass the `Github` repository build on a clean environment such as `Travis` by debugging the code locally.

Once the code is debugged, the next task is to add additional features to the code. One of these features may be inserting joint elements between elements of different materials. This would be particularly of interest for glass, considering the interface interaction between glass and PVB.

Only after the debugging and testing should it be necessary to involve the HPC systems, i.e. to produce simulations of greater scale.

ACKNOWLEDGMENTS

---

[15]g.gorman@imperial.ac.uk, Imperial College London, Department of Earth and Science
[16]y.ashton@imperial.ac.uk, Imperial College London, Department of Earth and Science

REFERENCES

[1] A. Stolz, O. Millon, C. Bedon, C. Kevin, A. V. Doormaal, C. Haberacker, M. Larcher, E. Commission, O. Millon, A. Saarenheimo, G. Solomos, E. Commission, and A. Stolz. 2015. *Recommendations for the Improvement of Existing European Norms for Testing the Resistance of Windows and Glazed Façades to Explosive Effects.* ISBN: 9789279533945. DOI: https://doi.org/10.2788/319252. https://ec.europa.eu/jrc/en/publication/recommendations-improvement-existing-european-norms-testing-resistance-windows-and-glazed-faades (cited on pages 1, 6).

[2] M. A. Samieian, D. Cormie, D. Smith, W. Wholey, B. R. Blackman, J. P. Dear, and P. A. Hooper. 2019. On the bonding between glass and PVB in laminated glass. *Engineering Fracture Mechanics*, 214, April, 504–519. ISSN: 00137944. DOI: https://doi.org/10.1016/j.engfracmech.2019.04.006. https://doi.org/10.1016/j.engfracmech.2019.04.006 (cited on pages 1, 3).

[3] W. Xu and M. Zang. 2014. Four-point combined DE/FE algorithm for brittle fracture analysis of laminated glass. *International Journal of Solids and Structures*, 51, 10, (May 2014), 1890–1900. ISSN: 00207683. DOI: https://doi.org/10.1016/j.ijsolstr.2014.01.026 (cited on pages 1, 3).

[4] C. D. Wu, X. Q. Yan, and L. M. Shen. 2014. A numerical study on dynamic failure of nanomaterial enhanced laminated glass under impact. In *IOP Conference Series: Materials Science and Engineering* number 1. Volume 10. Institute of Physics Publishing. DOI: https://doi.org/10.1088/1757-899X/10/1/012176 (cited on pages 1, 2, 7, 8).

[5] S. Chen, M. Zang, D. Wang, S. Yoshimura, and T. Yamada. 2017. Numerical analysis of impact failure of automotive laminated glass: A review. (August 2017). DOI: https://doi.org/

10.1016/j.compositesb.2017.04.007 (cited on page 1).

[6] F. W. Flocker and L. R. Dharani. 1998. Modeling interply debonding in laminated architectural glass subject to low velocity impact. *Structural Engineering and Mechanics*, 6, 5, 485–496. ISSN: 12254568. DOI: https://doi.org/10.12989/sem.1998.6.5.485 (cited on pages 1, 8).

[7] F. S. Ji, L. R. Dharani, and R. A. Behr. 1998. Damage probability in laminated glass subjected to low velocity small missile impacts. *Journal of Materials Science*, 33, 19, 4775–4782. ISSN: 00222461. DOI: https://doi.org/10.1023/A:1004457624817 (cited on pages 1, 8).

[8] X. Brajer, F. Hild, and S. Roux. 2010. On the dynamic fragmentation of glass: A meso-damage model. *International Journal of Fracture*, 163, 1-2, (May 2010), 121–131. ISSN: 03769429. DOI: https://doi.org/10.1007/s10704-009-9421-9 (cited on pages 1, 8).

[9] L. Monteleone, R. Steindler, and G. Kajon. 2004. Monitored ballistic tests on shockproof sandwich glasses in different conditions. *Experimental Techniques*, 28, 5, 28–32. ISSN: 07328818. DOI: https://doi.org/10.1111/j.1747-1567.2004.tb00183.x (cited on pages 1, 8).

[10] L. Biolzi, S. Cattaneo, and G. Rosati. 2010. Progressive damage and fracture of laminated glass beams. *Construction and Building Materials*, 24, 4, 577–584. ISSN: 09500618. DOI: https://doi.org/10.1016/j.conbuildmat.2009.09.007 (cited on page 1).

[11] P. J. G. Schreurs. 2012. Fracture Mechanics. Eindhoven, (September 2012). http://www.mate.tue.nl/~piet/edu/frm/pdf/frmsyl1213.pdf (cited on page 1).

[12] A. Munjiza, K. R. F. Andrews, and J. K. White. 1999. Combined single and smeared crack model in combined finite-discrete element analysis. *International Journal for Numerical Methods in Engineering*, 44, 1, (January 1999), 41–57. ISSN: 00295981. DOI: https://doi.org/10.1002/(SICI)1097-0207(19990110)44:1<41::AID-NME487>3.0.CO;2-A (cited on pages 2, 3).

[13] J. P. Latham, J. Xiang, A. Farsi, C. Joulin, N. Karantzoulis, A. Obeysekara, and P. Yang. 2019. Solidity Website. (2019). http://solidityproject.com/ (cited on pages 2, 4).

[14] A. Munjiza. 2004. *The Combined Finite-Discrete Element Method*. English. John Wiley & Sons, Ltd, Hoboken, 350. ISBN: 0470841990. DOI: https://doi.org/10.1002/0470020180. https://onlinelibrary.wiley.com/doi/book/10.1002/0470020180 (cited on pages 2–5).

[15] M. Abuaisha, D. W. Eaton, J. Priest, and R. Wong. 2015. Finite / Discrete Element Method (FDEM) by Y- Geo : An overview. *Microseismic Industry Consortium*, 5, February, 13. https://www.researchgate.net/publication/295705226_FiniteDiscrete_Element_Method_FDEM_by_Y-Geo_An_overview (cited on page 2).

[16] Q. Lei, J. P. Latham, and J. Xiang. 2016. Implementation of an Empirical Joint Constitutive Model into Finite-Discrete Element Analysis of the Geomechanical Behaviour of Fractured Rocks. *Rock Mechanics and Rock Engineering*, 49, 12, (December 2016), 4799–4816. ISSN: 0723-2632. DOI: https://doi.org/10.1007/s00603-016-1064-3. http://link.springer.com/10.1007/s00603-016-1064-3 (cited on pages 2, 4).

[17] X. Chen and A. H. Chan. 2018. Modelling impact fracture and fragmentation of laminated glass using the combined finite-discrete element method. *International Journal of Impact Engineering*, 112, (February 2018), 15–29. ISSN: 0734743X. DOI: https://doi.org/10.1016/j.ijimpeng.2017.10.007 (cited on pages 2, 3, 5–7).

[18] I. Mohagheghian, M. N. Charalambides, Y. Wang, L. Jiang, X. Zhang, Y. Yan, A. J. Kinloch, and J. P. Dear. 2018. Effect of the polymer interlayer on the high-velocity soft impact response of laminated glass plates. *International Journal of Impact Engineering*, 120,

(October 2018), 150–170. ISSN: 0734743X. DOI: https://doi.org/10.1016/j.ijimpeng.2018.06.002 (cited on pages 2, 8).

[19] X. e. Wang, J. Yang, Q. Liu, and C. Zhao. 2018. Experimental investigations into SGP laminated glass under low velocity impact. *International Journal of Impact Engineering*, 122, (December 2018), 91–108. ISSN: 0734743X. DOI: https://doi.org/10.1016/j.ijimpeng.2018.06.010 (cited on pages 2, 3, 8, 9).

[20] J. K. Kuntsche. 2015. *Mechanical behaviour of laminated glass under time-dependent and explosion loading*. German. Springer-Verlag Berlin Heidelberg, Darmstadt, 265. ISBN: 978-3-662-48830-0. DOI: https://doi.org/10.1007/978-3-662-48831-7 (cited on pages 2, 7).

[21] M. H. Ghadiri Rad, F. Shahabian, and S. M. Hosseini. 2015. A meshless local Petrov–Galerkin method for nonlinear dynamic analyses of hyper-elastic FG thick hollow cylinder with Rayleigh damping. *Acta Mechanica*, 226, 5, (May 2015), 1497–1513. ISSN: 0001-5970. DOI: https://doi.org/10.1007/s00707-014-1266-2. http://link.springer.com/10.1007/s00707-014-1266-2 (cited on pages 2, 3).

[22] N. H. Kim. 2015. *Introduction to nonlinear finite element analysis*. (1st edition). Springer, New York, NY, XIV, 430. ISBN: 9781441917461. DOI: https://doi.org/10.1007/978-1-4419-1746-1. https://www.springer.com/gp/book/9781441917454 (cited on page 2).

[23] Y. T. Gu, Q. X. Wang, and K. Y. Lam. 2007. A meshless local Kriging method for large deformation analyses. *Computer Methods in Applied Mechanics and Engineering*, 196, 9-12, 1673–1684. ISSN: 00457825. DOI: https://doi.org/10.1016/j.cma.2006.09.017 (cited on pages 2, 3).

[24] Abaqus. 2013. Abaqus Analysis User's Guide. (2013). http://ivt-abaqusdoc.ivt.ntnu.no:2080/v6.14/books/usb/default.htm (cited on pages 3, 7).

[25] N. Kumar and V. V. Rao. 2016. Hyperelastic Mooney-Rivlin Model : Determination and Physical Interpretation of Material Constants. *MIT International Journal of Mechanical Engineering*, 6, 1, 43–46. ISSN: 2230-7680. https://www.mitpublications.org/yellow_images/75618-me-book.43-46.pdf (cited on page 3).

[26] A. Munjiza, D. R. Owen, and N. Bicanic. 1995. A combined finite-discrete element method in transient dynamics of fracturing solids. *Engineering Computations*, 12, 2, (February 1995), 145–174. ISSN: 02644401. DOI: https://doi.org/10.1108/02644409510799532 (cited on page 3).

[27] A. Munjiza, E. E. Knight, and E. Rougier. 2012. *Computational mechanics of discontinua. Wiley series in computational mechanics*. Wiley, Chichester, West Sussex, U.K. DOI: https://doi.org/10.1002/9781119971160 (cited on page 3).

[28] A. Munjiza, Z. Lei, V. Divic, and B. Peros. 2013. Fracture and fragmentation of thin shells using the combined finite-discrete element method. *International Journal for Numerical Methods in Engineering*, 95, 6, 478–498. ISSN: 1097-0207. DOI: https://doi.org/10.1002/nme.4511. https://doi.org/10.1002/nme.4511 (cited on pages 3, 4).

[29] L. Guo, J. Xiang, J. P. Latham, and B. Izzuddin. 2016. A numerical investigation of mesh sensitivity for a new three-dimensional fracture model within the combined finite-discrete element method. *Engineering Fracture Mechanics*, 151, (January 2016), 70–91. ISSN: 00137944. DOI: https://doi.org/10.1016/j.engfracmech.2015.11.006 (cited on page 3).

[30] W. Gao and M. Zang. 2014. The simulation of laminated glass beam impact problem by developing fracture model of spherical DEM. *Engineering Analysis with Boundary Elements*, 42, 2–7. ISSN: 09557997. DOI: https://doi.org/10.1016/j.enganabound.2013.11.011 (cited on pages 3, 7).

[31] J. Xiang, A. Munjiza, and J. P. Latham. 2009. Finite strain, finite rotation quadratic tetrahedral element for the combined finite-discrete element method. *International Journal for Numerical Methods in Engineering*, 79, 8, (August 2009), 946–978. ISSN: 00295981. DOI: https://doi.org/10.1002/nme.2599 (cited on page 3).

[32] S. Chen, M. Zang, and W. Xu. 2015. A three-dimensional computational framework for impact fracture analysis of automotive laminated glass. *Computer Methods in Applied Mechanics and Engineering*, 294, (September 2015), 72–99. ISSN: 00457825. DOI: https://doi.org/10.1016/j.cma.2015.06.005. https://www.sciencedirect.com/science/article/pii/S0045782515001978 (cited on pages 4, 7, 8).

[33] GID. 2011. GID, The universal, adaptative and user friendly pre and post processing system for computer analysis in science and engineering. Reference Manual. (2011). http://www.compassis.com/downloads/Manuals/GiD_User_Manual.pdf (cited on page 5).

[34] J. Pelfrene, S. V. Dam, R. Sevenois, F. Gilabert, and W. v. Paepegem. 2016. Fracture Simulation of Structural Glass by Element Deletion in Explicit FEM. In *Challenging Glass 5 Conference on Architectural and Structural Applications of Glass* number July. Volume 5, 439–454. ISBN: 9789082526806. DOI: https://doi.org/10.7480/cgc.5.2270. https://www.researchgate.net/publication/304771271%20https://journals.open.tudelft.nl/index.php/cgc/article/view/2270 (cited on page 6).

[35] J. Xu, Y. Li, X. Chen, Y. Yan, D. Ge, M. Zhu, and B. Liu. 2010. Numerical study of PVB laminated windshield cracking upon human head impact. *Computers, Materials and Continua*, 18, 2, 183–211. ISSN: 1546-2218. DOI: https://doi.org/10.3970/cmc.2010.018.183. (cited on page 7).

[36] A. Vedrtnam and S. J. Pawar. 2017. Laminated plate theories and fracture of laminated glass plate - A review. *Engineering Fracture Mechanics*, 186, 316–330. ISSN: 00137944. DOI: https://doi.org/10.1016/j.engfracmech.2017.10.020 (cited on page 7).

[37] M. A. Samieian, D. Cormie, D. Smith, W. Wholey, B. R. Blackman, P. A. Hooper, and J. P. Dear. 2017. Delamination in Blast Resistant Laminated Glass. *21st International Conference on Composite Materials Xi'an, 20-25th August 2017*, August, 20–25. DOI: https://doi.org/10.1016/j.ijimpeng.2017.09.001 (cited on page 7).

[38] J. Stampfl and O. Koldenik. 2000. The separation of the fracture energy in metamaterials. *International Journal of Fracture*, 101, 321–345. DOI: https://doi.org/10.1023/A:1007500325074 (cited on page 7).

[39] M. Zang and S. Chen. 2012. Laminated glass. In (Second Edi edition). L. Nicolais and A. Borzacchiello, editors. Joh Wiley &, Guangzhou. DOI: https://doi.org/10.1002/9781118097298.weoc121 (cited on page 7).

[40] M. Sahin, C. S. Çetinarslan, and H. E. Akata. 2007. Effect of surface roughness on friction coefficients during upsetting processes for different materials. *Materials and Design*, 28, 2, 633–640. ISSN: 18734197. DOI: https://doi.org/10.1016/j.matdes.2005.07.019 (cited on page 7).

[41] M. Fahlbusch. 2007. Zur Ermittlung der Resttragfähigkeit von Verbundsicherheitsglas am Beispiel eines Glasbogens mit Zugstab. German, (March 2007), 1–123. http://elib.tu-darmstadt.de/diss/000962 (cited on page 7).

[42] A. Farsi and J. Xiang. 2019. DEM Plus Manual. (2019) (cited on page 6).

[43] J. Zucker, J. Brades, A. New, and A. Toon. 2016. Jabisupra Company Website. (2016). https://www.jabisupra.co.uk/ (cited on page 8).

[44] I. Mohagheghian, Y. Wang, J. Zhou, L. Yu, X. Guo, Y. Yan, M. N. Charalambides, and J. P. Dear. 2017. Deformation and damage mechanisms of laminated glass windows subjected to high velocity soft impact. *International*

Journal of Solids and Structures, 109, (March 2017), 46–62. ISSN: 00207683. DOI: https://doi.org/10.1016/j.ijsolstr.2017.01.006 (cited on page 8).

[45] P. Grant, W. Cantwell, H. McKenzie, and P. Corkhill. 1998. The Damage Threshold Of Laminated Glass Structures. *International Journal of Impact Engineering*, 21, 9, (October 1998), 737–746. ISSN: 0734743X. DOI: https://doi.org/10.1016/s0734-743x(98)00027-x (cited on page 8).

[46] K. A. D. L. P. Karunarathna. 2013. Low-Velocity Impact Analysis Of Monolithic And Laminated Glass Using Finite Element Method (FEM). March. https://etheses.bham.ac.uk/id/eprint/5067/2/Kuruvita14MPhil.pdf (cited on page 8).

[47] U. A. Dar, W. Zhang, and Y. Xu. 2013. FE Analysis of Dynamic Response of Aircraft Windshield against Bird Impact. *International Journal of Aerospace Engineering*, 2013, (May 2013), 1–12. ISSN: 1687-5966. DOI: https://doi.org/10.1155/2013/171768 (cited on page 8).

[48] X. Zhang, I. K. Mohammed, M. Zheng, N. Wu, I. Mohagheghian, G. Zhang, Y. Yan, and J. P. Dear. 2019. Temperature effects on the low velocity impact response of laminated glass with different types of interlayer materials. *International Journal of Impact Engineering*, 124, (February 2019), 9–22. ISSN: 0734743X. DOI: https://doi.org/10.1016/j.ijimpeng.2018.09.004 (cited on pages 8, 9).

[49] F. Mili. 2012. Effect of the Impact Velocity on the Dynamic Response of E-Glass/Epoxy Laminated Composites. *Arabian Journal for Science and Engineering*, 37, 2, (March 2012), 413–419. ISSN: 13198025. DOI: https://doi.org/10.1007/s13369-012-0174-9 (cited on page 8).

[50] R. A. Behr, P. A. Kremer, L. R. Dharani, F. S. Ji, and N. D. Kaiser. 1999. Dynamic strains in architectural laminated glass subjected to low velocity impacts from small projectiles. *Journal of Materials Science*, 34, 23, (December 1999), 5749–5756. ISSN: 00222461. DOI: https://doi.org/10.1023/A:1004702100357 (cited on pages 8, 9).

[51] B. Liu, T. Xu, X. Xu, Y. Wang, Y. Sun, and Y. Li. 2016. Energy absorption mechanism of polyvinyl butyral laminated windshield subjected to head impact: Experiment and numerical simulations. *International Journal of Impact Engineering*, 90, (April 2016), 26–36. ISSN: 0734743X. DOI: https://doi.org/10.1016/j.ijimpeng.2015.11.010 (cited on page 9).

[52] B. H. Kim, K. C. Ahn, and C. W. Lee. 2016. Low Velocity Impact Behaviors of a Laminated Glass. *Smart Science*, 2, 4, (June 2016), 209–213. DOI: https://doi.org/10.1080/23080477.2014.11665628 (cited on page 9).

[53] Kitware. [n. d.] Visualisation Toolkit. (). vtk.org (cited on pages 9, 10, 16).

[54] H.-P. Bunge. 2009. Earth Models. Munich, (March 2009). http://www.earthmodels.org (cited on pages 9–11, 16).

[55] J. Aspnes. 2014. C/FloatingPoint. New Haven, Conneticut, (2014). http://www.cs.yale.edu/homes/aspnes/pinewiki/C(2f)FloatingPoint.html (cited on page 11).

[56] D. Apps. [n. d.] Simple online tools. https://www.pinterest.co.uk/davinapps/simple-online-tools/ (cited on page 12).

[57] J. Malinen. [n. d.] B64 encoding function. (). http://web.mit.edu/freebsd/head/contrib/wpa/src/utils/base64.c (cited on page 13).

[58] C. Geuzaine and J.-F. Remacle. 2009. Gmsh: a three-dimensional finite element mesh generator with built-in pre- and post-processing facilities. http://gmsh.info/ (cited on page 16).

[59] A. Munjiza. 2000. Manual for the " Y " Fem / Dem Computer Program. C, 1–19.